Triggering and Restabilization of Combustion Instability with Rocket Motor Acceleration

Pavel P. Popov,* Athanasios Sideris,† and William A. Sirignano‡
University of California, Irvine, Irvine, California 92697

The probability of a liquid-propulsion rocket motor to develop screeching instability is studied computationally. The combustion chamber is accelerated as a rigid body using a prescribed acceleration time history; it is found that accelerations of proper magnitude, duration, and frequency induce a pressure wave inside the combustion chamber that grows to a screeching acoustic wave limit cycle. For a rectangular rocket motor, a reciprocating transverse acceleration leads to the development of a transverse pressure wave limit cycle; for a cylindrical rocket motor, the limit cycle may be either a standing wave, for a transverse reciprocating acceleration, or a spinning wave, for a transverse rotating acceleration. It is found that a limit cycle may be induced by either a large acceleration pulse of short duration or a smaller acceleration pulse of a longer duration. The polynomial chaos expansion method is used to study the probability of growth to a limit-cycle oscillation when the amplitude and frequency of the transverse acceleration pulse are random.

Nomenclature

a	=	speed of sound, m/s
$a^C(t)$	=	acceleration time history, m/s^2
c_p	=	specific heat at constant pressure, J/(°K kg)
D	=	mass diffusivity, m^2/s
E	=	energy release rate, J/kg · s
F_i	=	inertial volumetric force, N/m
L	=	chamber thickness, m
p	=	pressure, N/m^2
R_c	=	chamber wall radius of curvature, m
r	=	radial position, m
T	=	temperature, K
t	=	time, s
u	=	fluid velocity, m/s
$\hat{x}$	=	unit vector in x direction
$\hat{y}$	=	unit vector in y direction
Y_i	=	mass fraction of species i
α, β	=	Schwab-Zel'dovich variables
γ	=	ratio of specific heats
η	=	local radial coordinate for injector grids
ν_T	=	turbulent kinematic viscosity, m^2/s
ρ	=	density, kg/m^3
ω_i	=	reaction rate of species i, m^{-1}

Subscripts

F	=	fuel
i	=	index for chemical species
i, j	=	index for Cartesian coordinates
O	=	oxidizer
0	=	undisturbed state

*Postdoctoral Researcher, Department of Mechanical and Aerospace Engineering. Member AIAA.
†Professor, Department of Mechanical and Aerospace Engineering.
‡Professor, Department of Mechanical and Aerospace Engineering. Fellow AIAA.

I. Introduction

ACOUSTIC combustion instability of liquid-propellant rocket engines is a well known and potentially destructive phenomenon that occurs when existing acoustic disturbances within a combustion chamber are amplified by the energy release of combustion [1,2]. The resulting acoustic oscillations typically lead to heat damage to the rocket engine, due to hot products from the combustion chamber's interior being brought into closer proximity of the chamber walls.

The typical combustion instability setting occurs for motors that are linearly stable, so that small disturbances decay, but may develop an instability for a large enough perturbation, usually caused by an unforeseen event. Previously, it has been demonstrated that such disturbances can come in the form of an acoustic wave within the combustion chamber [3], a localized pressure pulse that models a bombing experiment [4], or a blockage in one of the rocket motor injector ports [5]. All of these mechanisms share the characteristic that they originate within the rocket engine (either in the combustion chamber or injector ports) and may thus be observed either on a test stand experiment or in flight.

For several rocket engine designs that exhibit no combustion instability in test stand experiments, behavior suggesting combustion instability is observed in flight.§ This suggests that external acceleration imposed on the rocket motor, due to in-flight vibration and aerodynamic forces, is an important potential mechanism for instability generation in otherwise stable engine designs. This study focuses on the exploration of this mechanism for combustion instability.

In this work, we consider the effects of externally imposed acceleration on two different types or rocket motors: a ten-injector rocket engine with a cylindrical combustion chamber and a seven-injector rocket engine with a rectangular combustion chamber. The latter of these two is based on an experimental setup at Purdue University [6], with modified inflow conditions chosen so that the overall system is conditionally unstable. The original experimental conditions, which cause unconditional transverse instability of the rocket motor, have also been simulated using the present code, with the results presented in [7]. That study observed good agreement between simulation and experiment, validating the present modelling and computational approach.

The ten-injector cylindrical rocket engine was previously studied and shown to be conditionally unstable, with a limit-cycle instability that could be triggered by a preexisting pressure wave [3], a pressure pulse [4], and an injector blockage [5]. The combustion chamber is a cylinder of which the length is $L = 0.5$ m and of which the radius is $R = 0.14$ m, with the injectors distributed in three rings, with one

Axisymmetric cylindrical grid for injectors

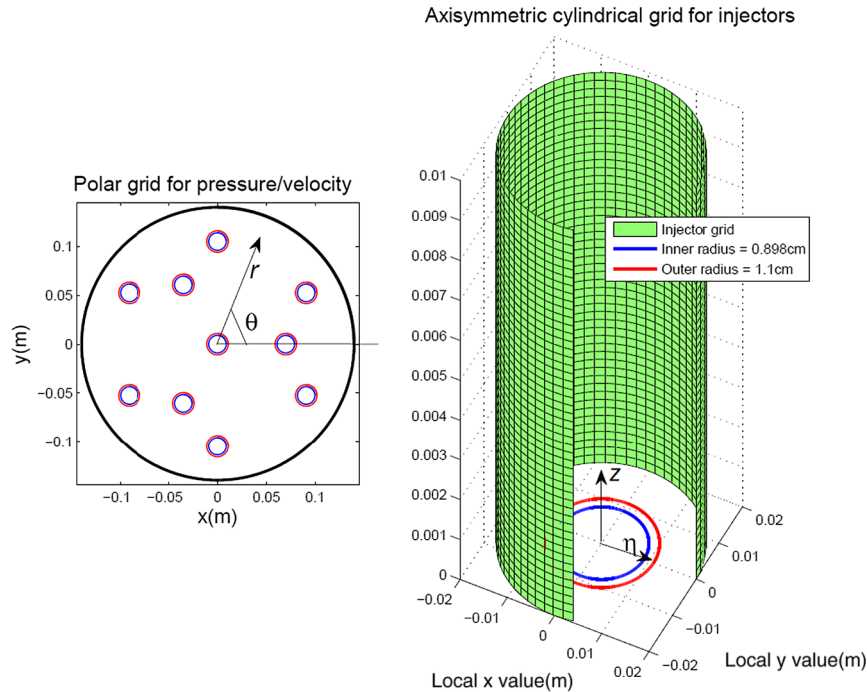Polar grid for pressure/velocity

Fig. 1   Left: cylindrical combustion chamber and injector distribution. Right: axisymmetric cylindrical grid used for the solution of each of the ten injector jet flames.

injector at the center of the chamber, three injectors at a radius of $r = R/2$, and the remaining six injectors spread evenly at a radius of $r = 3R/4$ from the center (see Fig. 1).

Each injector consists of two concentric ports, the inner of which serves as the oxidizer port and has a radius of 0.898 cm, and the outer, annular port has an inner radius of 0.898 cm and an outer radius of 1.1 cm and serves as the fuel inlet. Both fuel and oxidizer injector ports have a length of 11.5 cm. For this case, the fuel is CH_4, the oxidizer is O_2, and the mean pressure inside the combustion chamber at standard operating conditions is 200 atm. For more details of this computational configuration, the reader is referred to [3,5]. The injector inlets are modeled as pressure-driven inflows, with a fixed-pressure inlet manifold separated from the injector inlets by an obstruction of the fixed discharge coefficient [5,7]. Therefore, acoustic coupling between the inlet manifold and the combustion chamber is approximated as negligible.

With x, y being the transverse directions as shown on the left of Fig. 1, we consider two types of combustion chamber acceleration time histories; in both of these cases, only the chamber's position changes, not its orientation. In Case 1, the acceleration is given by

$$\boldsymbol{a}^C = A_0 \cos(-\omega t)\hat{\boldsymbol{x}} + A_0 \sin(-\omega t)\hat{\boldsymbol{y}} \qquad (1)$$

so that the acceleration vector rotates circularly in the chamber transverse direction. As we shall later see, this type of acceleration may produce a spinning wave limit cycle. The parameters that describe a given acceleration time history are its amplitude A_0, angular frequency ω, and length T of the acceleration period; for $t > T$, the chamber is not further perturbed.

In Case 2, the acceleration is given by

$$\boldsymbol{a}^C = A_0 \sin(-\omega t)\hat{\boldsymbol{y}} \qquad (2)$$

which describes a reciprocating vector in the y direction that may induce a standing wave limit cycle.

The second rocket engine considered in this work has a rectangular combustion chamber with seven injectors (see Fig. 2). The geometry
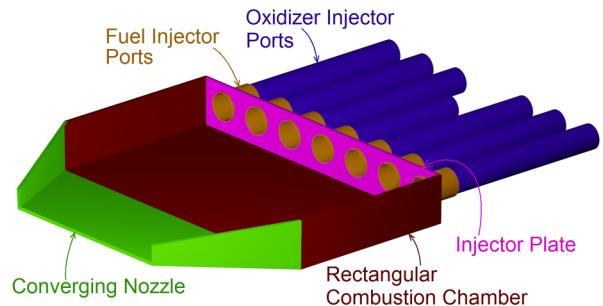

Fig. 2   Geometry of the rectangular seven-injector rocket motor and propellant ports.

and propellants are the same as described in [8] for the "OOXOXOO" case: the central port of each injector runs a mixture of 58% H_2O and 42% O_2 as the oxidizer, with the fuel in the central injector being C_2H_6, the fuel in the outer two injectors on each side being $RP1$ (here modelled as decane), and the injectors on both sides of the central one having no fuel inflow.

A departure is made from the experimental conditions in that the propellant mass flow rate is reduced by 30 to 70% of the experimental values. For this mass flow rate, the numerical algorithm described in the following section predicts a conditionally unstable system, whereas for the original experimental values, both the experimental data and numerical calculations [7] indicate an unconditionally unstable engine. As the object of this study is to determine which acceleration perturbations may destabilize an otherwise stable engine, the mass flow modification is justified.

The acceleration specification for the rectangular chamber is analogous to Case 2 for the cylindrical chamber. Namely, the acceleration time history follows Eq. (2), where $\hat{\boldsymbol{y}}$ is the transverse direction of the combustion chamber, over which the injectors are spread. With this specification, an acceleration pulse of sufficient magnitude and length, and frequency close to that of a first transverse acoustic mode, may cause the development of an acoustic wave limit cycle.

II. Wave Dynamics Equations

There are several simplifications that can be made for the equations of pressure and velocity. Because the scale of the turbulent motions is much smaller than the acoustic wave scale, we can assume that turbulence and molecular diffusion do not have a considerable influence over the large-scale pressure and velocity wave fields. Therefore, the pressure and velocity wave fields can be solved in inviscid form.

A. Wave Equations Without Acceleration

Following [3], the chamber pressure wave equation has the form

$$\frac{\partial^2 p}{\partial t^2} - a^2 \frac{\partial^2 p}{\partial x_j \partial x_j} = \frac{\partial \rho}{\partial t} \frac{\partial a^2}{\partial t} + (\gamma - 1) \frac{\partial E}{\partial t} + a^2 \frac{\partial^2 (\rho u_j u_i)}{\partial x_i \partial x_j} \quad (3)$$

The left-hand side of the equation represents the wave operator in three dimensions. The second term on the right represents the influence of the combustion energy release on the acoustic instability and is thus an integral component of the study of rocket engine instability.

The large-scale velocity components evolve by

$$\frac{\partial u_i}{\partial t} + u_j \frac{\partial u_i}{\partial x_j} + \frac{C}{p^{1/\gamma}} \frac{\partial p}{\partial x_i} = 0 \quad (4)$$

where $C = p_0^{1/\gamma}/\rho_0$, and the assumption is made that pressure dominates over the turbulent and molecular viscosity terms.

These equations are applied to both the cylindrical and rectangular combustion chambers by averaging over one of the spatial directions, along which there is little variation of the pressure and velocity fields. For the cylindrical chamber simulations, which focus on transverse instabilities, averaging is performed in the axial direction [5]; for the rectangular chamber cases, the averaging is done across the short vertical distance in Fig. 2 [7].

B. Effect of Acceleration on Combustion Chamber Wave Equations

In this work, we solve for pressure and velocity in a reference frame fixed to the combustion chamber, which undergoes irrotational acceleration $\boldsymbol{a}_C(t)$. Therefore, in the accelerating frame, the fluid experiences the inertial (volumetric) force

$$F_i = -\rho \boldsymbol{a}^C(t) \quad (5)$$

This inertial body force acting on the fluid modifies the momentum equation, which becomes

$$\frac{\partial u_i}{\partial t} + u_j \frac{\partial u_i}{\partial x_j} + \frac{C}{p^{1/\gamma}} \frac{\partial p}{\partial x_i} + a_i^c = 0 \quad (6)$$

as well as the pressure wave equation, which, in the noninertial frame, has the form

$$\frac{\partial^2 p}{\partial t^2} - a^2 \frac{\partial^2 p}{\partial x_j \partial x_j} = \frac{\partial \rho}{\partial t} \frac{\partial a^2}{\partial t} + (\gamma - 1) \frac{\partial E}{\partial t} + a^2 \frac{\partial^2 (\rho u_j u_i)}{\partial x_i \partial x_j} + a^2 \frac{\partial \rho}{\partial x_i} a_i^C \quad (7)$$

Additionally, the inertial force modifies the pressure boundary condition at the chamber walls, the form of which is

$$\frac{\partial p}{\partial n} = \frac{p^{1/\gamma} u_t^2}{CR_c} - \frac{p^{1/\gamma} a_n^C}{C} \quad (8)$$

where u_t is the velocity component tangential to the boundary, R_c is the wall boundary radius of the curvature, and n and a_n^C are the unit outward normal vector at the boundary and the component of the acceleration in that direction, respectively.

In this study, we use the fact that the rectangular combustion chamber is narrow in the height dimension, which implies that the solution fields vary little in that dimension and can therefore be averaged over it. The chamber height $L(x, y)$ is constant over the initial section of the combustion chamber and varies linearly with x in the converging nozzle portion of the chamber.

Following Sirignano and Popov [3], two-dimensional averages are made (here, over the height dimension) of the pressure and velocity fields $\tilde{p} = (1/L(x, y)) \int_0^{L(x,y)} p \, dz$, $\tilde{\rho} = (1/L(x, y)) \int_0^{L(x,y)} \rho \, dz$, $\tilde{a} = (1/L(x, y)) \int_0^{L(x,y)} a \, dz$, and $\tilde{\boldsymbol{u}} = (1/L(x, y)) \int_0^{L(x,y)} \boldsymbol{u} \, dz$. Integrating Eq. (3) over z and neglecting the difference between products of averages and averages of products, we get

$$\frac{\partial^2 \tilde{p}}{\partial t^2} - \tilde{a}^2 \left[\frac{\partial^2 \tilde{p}}{\partial x_j \partial x_j} + \frac{1}{L} \frac{\partial L}{\partial x_1} \frac{\partial \tilde{p}}{\partial x_1} \right] = \frac{\partial \tilde{\rho}}{\partial t} \frac{\partial \tilde{a}^2}{\partial t} + (\gamma - 1) \frac{\partial \tilde{E}}{\partial t} +$$
$$+ \tilde{a}^2 \frac{\partial^2 (\tilde{\rho} \tilde{u}_j \tilde{u}_i)}{\partial x_i \partial x_j} + \tilde{a}^2 \frac{1}{L} \frac{\partial L}{\partial x_1} \frac{\partial (\tilde{\rho} \tilde{u}_1 \tilde{u}_i)}{\partial x_i} \quad (9)$$

where $i = 1, 2$; $j = 1, 2$. The last terms on both the left- and right-hand sides correspond to the effect that the variable combustion chamber width (in the x_3 direction) has on the divergence operators in Eq. (3). The previous equation contains derivatives of L only in the x_1 direction because L does not vary in the x_2 direction.

Similarly, the averaged version of Eq. (4) has the form

$$\frac{\partial \tilde{u}_i}{\partial t} + \tilde{u}_j \frac{\partial \tilde{u}_i}{\partial x_j} + \frac{1}{L} \frac{\partial L}{\partial x_1} (\tilde{u}_i \tilde{u}_1) + \frac{C}{\tilde{p}^{1/\gamma}} \frac{\partial \tilde{p}}{\partial x_i} = 0 \quad (10)$$

These equations are solved on an orthogonal curvilinear coordinate system, which represents a conformal map of the present hexagonal domain onto a square. The curvilinear form of Eqs. (9) and (10), with the associated nomenclature, is given in Appendix A.

At the walls of the combustion chamber, the boundary conditions on the pressure and velocity are

$$\tilde{u}_n = 0; \qquad \frac{\partial \tilde{p}}{\partial n} = \frac{\tilde{p}^{1/\gamma} \tilde{u}_t^2}{CR_c} \quad (11)$$

with $\tilde{u}_n$, $\tilde{u}_t$ denoting the components of velocity normal and tangential to the wall boundary, respectively, and R_c denoting the wall boundary's radius of curvature. At the downstream end of the convergent nozzle, a Mach number $M = 0.9$ is enforced for the rectangular chamber case, and the short nozzle approximation [9] is used to represent the additional convergence to a choked throat, as an approximation to the sonic condition in the experiment. This is done for the sake of accuracy and numerical stability, as the present code is designed for subsonic flows. When compared to the acoustic length scale (the chamber width), the distance between the $M = 0.9$ and $M = 1.0$ locations is negligible and thus also is the approximation error caused by treating this region as a short nozzle.

III. Additional Model Equations

We seek to model the heat release rate of change, $\partial E/\partial t$, which is an integral component to the acoustic instability pressure wave equation, Eq. (3). Following [3], we shall denote $\alpha = Y_F - \nu Y_O$, where Y_F, Y_O are the fuel and oxidizer mass fractions, and ν is their stoichiometric ratio. Then, α is a conserved scalar, which we will determine in the vicinity of each injector, on an axisymmetric cylindrical grid with the assumption that the injector flow field is mostly in the direction axial to the injector.

With the variable β being defined by $\beta = (Q/(c_p T_o)) Y_F + T/T_o - (p/p_o)^{(\gamma-1)/\gamma}$, the evolution equations for the variables α, β, Y_F have the form

$$\frac{\partial \alpha}{\partial t} + u_x \frac{\partial \alpha}{\partial z} + u_\eta \frac{\partial \alpha}{\partial \eta} - D \left[\frac{\partial^2 \alpha}{\partial \eta^2} + \frac{1}{\eta} \frac{\partial \alpha}{\partial \eta} + \frac{\partial^2 \alpha}{\partial z^2} \right] = 0 \quad (12)$$

$$\frac{\partial \beta}{\partial t} + u_z \frac{\partial \beta}{\partial z} + u_\eta \frac{\partial \beta}{\partial \eta} - D\left[\frac{\partial^2 \beta}{\partial \eta^2} + \frac{1}{\eta}\frac{\partial \beta}{\partial \eta} + \frac{\partial^2 \beta}{\partial z^2}\right] = 0 \quad (13)$$

and

$$\frac{\partial Y_F}{\partial t} + u_z \frac{\partial Y_F}{\partial z} + u_\eta \frac{\partial Y_F}{\partial \eta} - D\left[\frac{\partial^2 Y_F}{\partial \eta^2} + \frac{1}{\eta}\frac{\partial Y_F}{\partial \eta} + \frac{\partial^2 Y_F}{\partial z^2}\right] = \omega_F$$

$$(14)$$

where z and h are the axial and radial coordinates of the cylindrical injector grids, respectively, and the source term on the right-hand side of Eq. (14) is obtained from a Westbrook–Dryer two-step oxidation mechanism [10], from the fuel (C_2H_6 for the central injector element and $C_{10}H_{22}$ for the driving injector elements) to CO and then from CO to CO_2. To obtain the concentrations of both the injector fuel and CO from the fuel mass fraction, it is assumed that the oxidation of CO occurs only after the partial oxidation of the fuel to CO has reached its completion.

Building on [3], the source term in Eq. (14) is obtained via an assumed-probability density function (PDF) model for α and β so that the means of α and β evolve by Eqs. (12) and (13) and their subgrid distributions are assumed to be beta functions, which are standard PDFs for modeling mixing of two or more streams. The term ω_F in Eq. (14) is then obtained via integration over the sample space of α and β. The assumed PDF model has been used with great success for the simulation of turbulent nonpremixed flames that are not near extinction [11]. For more details, the reader is referred to [11].

The axial and radial velocities in Eqs. (12–14) are obtained from a solution of the variable density Reynolds-averaged Navier–Stokes axisymmetric equations,

$$\rho\left(\frac{\partial u_z}{\partial t} + u_z \frac{\partial u_z}{\partial z} + u_\eta \frac{\partial u_z}{\partial \eta}\right) = -\frac{\partial p_l}{\partial z} + \rho\nu_T\left[\frac{\partial^2 u_z}{\partial z^2} + \frac{1}{\eta}\frac{\partial}{\partial \eta}\left(\eta \frac{\partial u_z}{\partial \eta}\right)\right]$$

$$(15)$$

$$\rho\left(\frac{\partial u_\eta}{\partial t} + u_z \frac{\partial u_\eta}{\partial z} + u_\eta \frac{\partial u_\eta}{\partial \eta}\right) = -\frac{\partial p_l}{\partial \eta} + \rho\nu_T\left[\frac{\partial^2 u_\eta}{\partial z^2} + \frac{1}{\eta}\frac{\partial}{\partial \eta}\left(\eta \frac{\partial u_\eta}{\partial \eta}\right) - \frac{u_\eta}{\eta^2}\right]$$

$$(16)$$

which are solved on each jet flame grid, where $p_l(z, \eta, t)$ is a local hydrodynamic pressure of which the mean is by definition zero and that has a considerably lower magnitude than the injector pressure $p(t)$ obtained from Eq. (3). The density in Eqs. (16) and (17) is obtained from the species scalars and the long-wavelength pressure $p(t)$ at the injector's location so that the overall procedure for solving Eqs. (16) and (17) is elliptic.

Finally, following Popov et al. [5], the pressure and velocity in the injector posts are solved via the set of one-dimensional wave equations:

$$\frac{\partial^2 p}{\partial t^2} - a^2 \frac{\partial^2 p}{\partial l^2} = a^2 \frac{\partial^2 (\rho u^2)}{\partial l^2} - \frac{\partial a^2}{\partial t}\frac{\partial(\rho u)}{\partial l} \quad (17)$$

$$\frac{\partial u}{\partial t} + u \frac{\partial u}{\partial l} = -\frac{1}{\rho}\frac{\partial p}{\partial l} \quad (18)$$

They are solved on a one-dimensional grid upstream of each cylindrical injector grid. In this model, velocity fluctuations affect the energy release rate through the modification of the eddy diffusivity,

mixing rate, and the rate of propellant inflow into the combustion chamber. Pressure fluctuations, on the other hand, affect the chemical rate and drive the injector port velocity fluctuations.

For initial conditions to the model equations described in this and the prior sections, the authors use a steady-state solution of an unperturbed combustion chamber. Since the present study deals with conditionally unstable (i.e., stable to small disturbances) configurations, a steady-state solution can be obtained without special treatment of the rocket motor startup.

IV. Deterministic and Stochastic Acceleration of Cylindrical Rocket Motor

For both cases, rotating and reciprocating acceleration, we set the angular frequency ω to $2\pi/\tau_F$, where $\tau_F = 0.478$ ms is the period of the first tangential acoustic mode of the combustion chamber. Setting the period to $T = 2\tau_F$ and varying the amplitude A_0, we run several calculations for both Cases 1 and 2. The resulting pressure wave amplitudes at the end of the simulation are plotted as functions of A_0 on Fig. 3.

As can be seen in that figure, an amplitude above $A_0 = 1900$ m/s^2 causes an acoustic instability for Case 1, and an amplitude above $A_0 = 3100$ m/s^2 causes the growth of an acoustic instability in Case 2. Both types of instabilities have the shape of a first tangential acoustic mode, with the difference that in Case 1 the wave is spinning whereas in Case 2 it is standing. It is important to note that the spinning acceleration pulse of Case 1 can cause an instability at a lower amplitude, due to the larger L^2 norm of $\boldsymbol{a}^C(t)$ for a set A_0 in Case 1.

Figure 4 shows the development of a spinning acoustic wave in Case 1. It is interesting to note that at the early stages of the limit cycle's development the pressure perturbations are localized near the chamber walls. This is due to the fact that, with the present model, the density throughout the combustion chamber is initially uniform so that the density gradient term $a^2(\partial\rho/\partial x_i)a_i^C$ in Eq. (7) is equal to zero. Rather, the initial disturbance in the pressure field comes about due to the inertial force term in the boundary condition, Eq. (8), so that the pressure disturbance spreads inward from the walls.

As a companion to Fig. 4, in Fig. 5 we include a longitudinal cross-section, along the plane defined by $x = 0$, which also includes three of the ten injectors. This figure illustrates clearly how the pressure disturbance propagates inward from the walls, and then upstream into the injector ports, once an injector is reached.

An acceleration pulse has the capability to not only cause the development of a limit cycle but to also suppress it. Specifically, for all the cases from Fig. 3, adding an additional pulse of duration $T = 2\tau_F$ and frequency $\omega = 2\pi/\tau_F$, but of amplitude $-A_0$, succeeded in arresting the growth of the acoustic instability. This
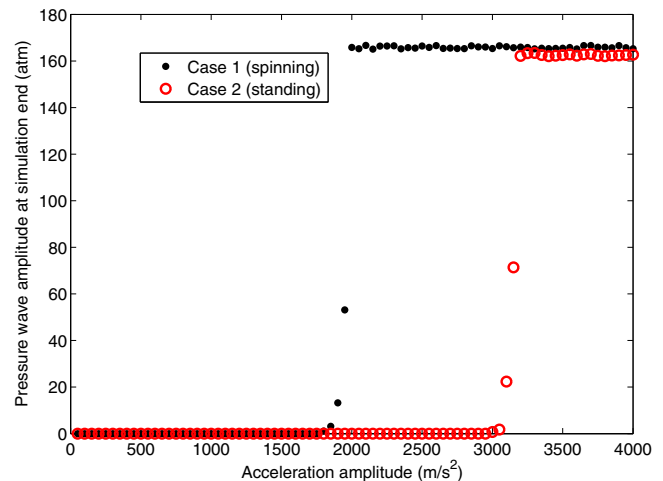

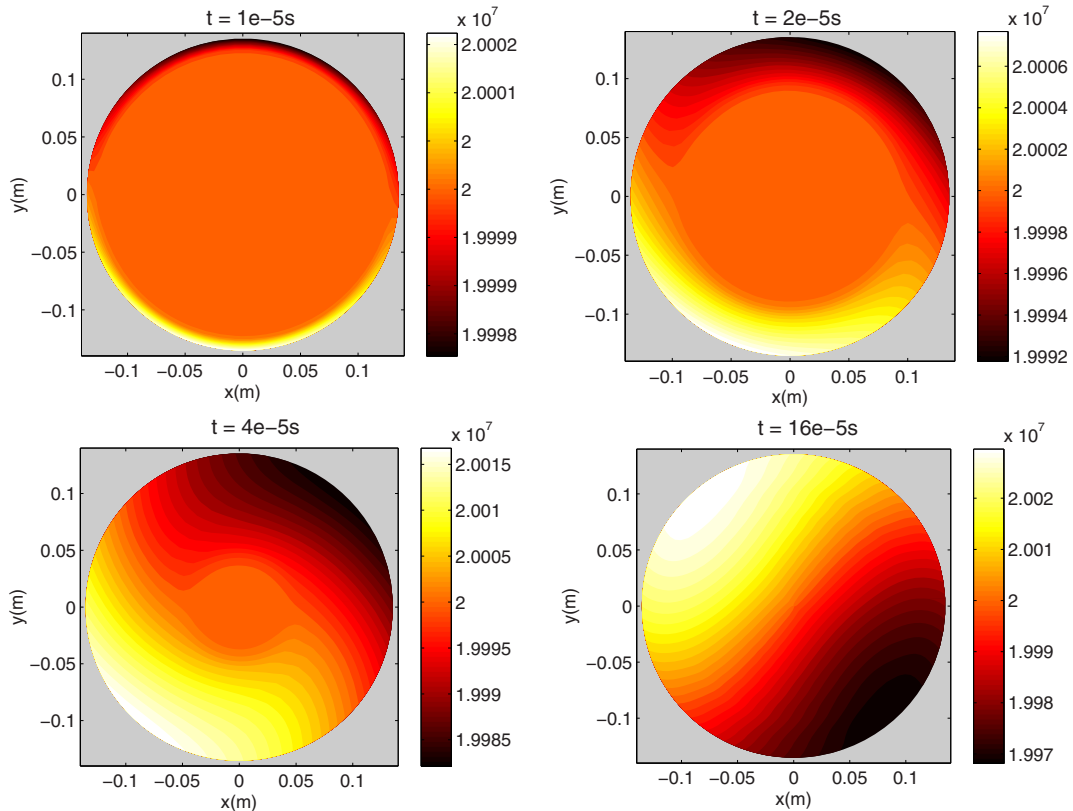Fig. 3 Final pressure wave amplitude as a function of acceleration amplitude.

Fig. 4   Initial stages of development of a spinning acoustic wave (spin direction is clockwise). Pascals are the contour units.

finding is consistent with earlier results [4,7] in which other pulsing mechanisms could provide stabilization. In the next section, we also consider cases when the "antipulse" occurs after some delay.

In addition to the deterministic simulations described previously, we also perform a polynomial chaos expansion (PCE) [4] solution for the cylindrical rocket motor. The stochastic parameters
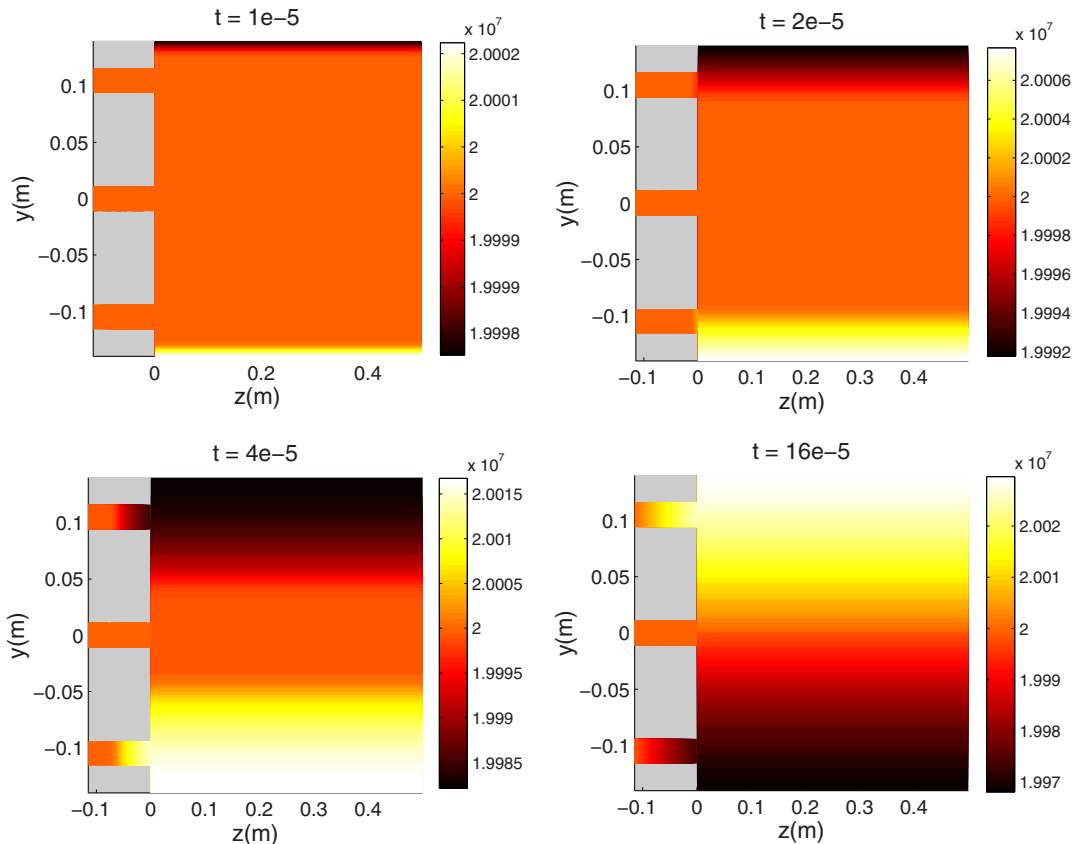
Fig. 5   Initial stages of development of a spinning acoustic wave: longitudinal cross-section at the plane defined by $x = 0$. Pascals are the contour units.

in this case are the pulse's acceleration amplitude $A_0 \in [500 \text{ m/s}^2, 4500 \text{ m/s}^2]$, duration $T \in [0, 1.6 \times 10^{-3} \text{ s}]$, and frequency $f \in [1400 \text{ Hz}, 2800 \text{ Hz}]$. The values of A_0, T and f are uniformly distributed in these intervals and are independent of each other.

To determine the effect of each of those variables on the overall stability of the rocket motor, we calculate the marginal probability, for each of the three sample space variables, of the growth of the initial disturbance to an instability. As a specific example, the marginal probability of growth to instability as a function of a given sample space variable ξ_i is calculated by integrating over the remaining sample space variables in the vector,

$$P_{\text{growth}}(\xi_i) = \int \chi_{\text{growth}}(\xi) f(\xi) |\, d\xi_{j \neq i}| / f(\xi) |\, d\xi_{j \neq i}| \qquad (19)$$

where $f(\xi)$ is the probability density function (in this case, a uniform distribution) and $\chi_{\text{growth}}(\xi)$ is the indicator function of a solution growing to instability: $\chi_{\text{growth}}(\xi) = 1$ when instability develops for a given ξ and $\chi_{\text{growth}}(\xi) = 0$ otherwise. The integration in Eq. (19) is performed via a Smolyak grid quadrature.

Figure 6 shows a plot of the marginal probability, as a function of A_0, of growth to an instability. As can be expected, the probability of growth increases monotonically with the acceleration amplitude, with larger increments around $A_0 = 2500 \text{ m/s}^2$.

The probability of growth as a function of the pulse duration is shown on Fig. 7. On that figure, it can be observed that the probability of growth rises monotonically with increasing duration. We note, however, that the increase of the probability is more gradual than on Fig. 6.

This can be attributed to the dissipation of acoustic waves that have not risen above the threshold for triggering: increasing the duration of an acceleration pulse increases the amount of dissipation that the
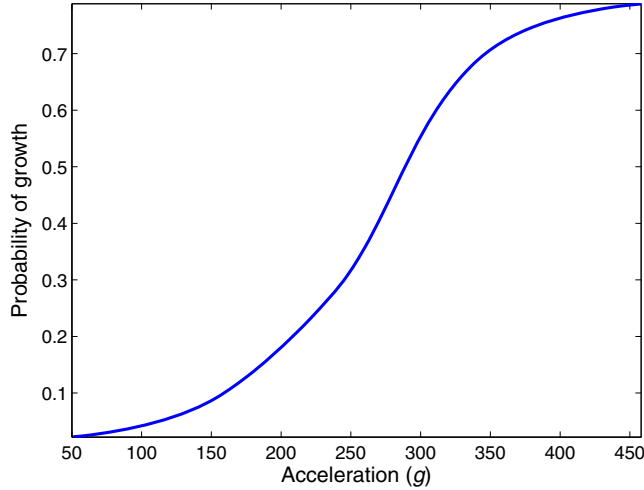

Fig. 6 Marginal probability of growth to an instability as a function of the acceleration pulse's amplitude, in gravity.
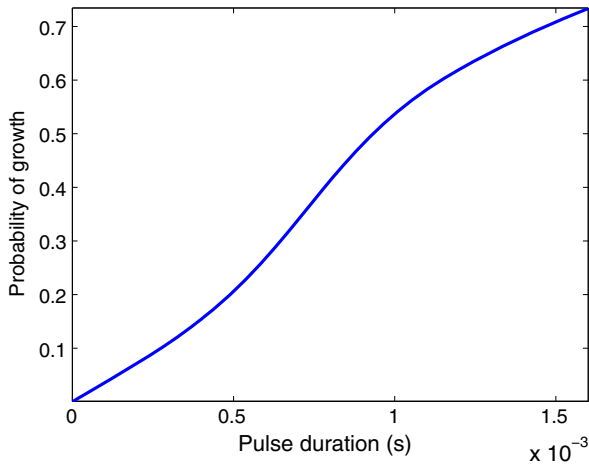

Fig. 7 Marginal probability of growth to an instability as a function of the acceleration pulse's duration, in seconds.
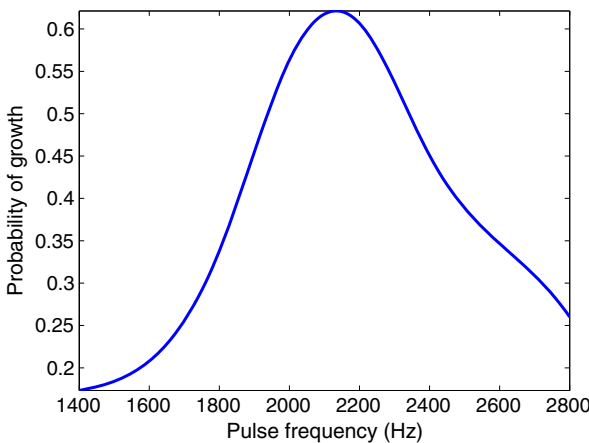

Fig. 8 Marginal probability of growth to an instability as a function of the acceleration pulse's frequency, in hertz.
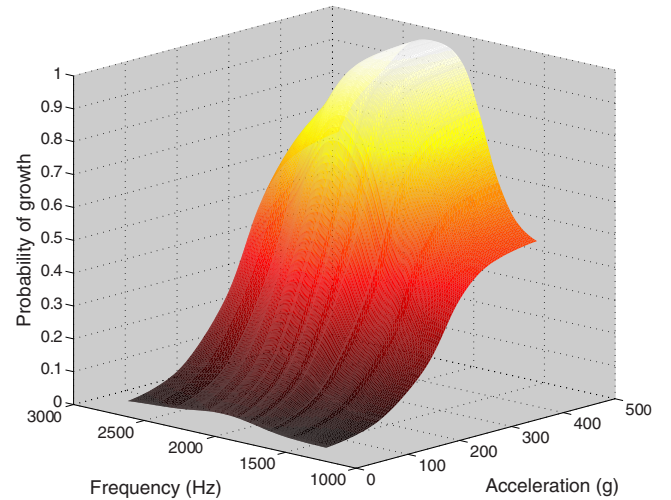

Fig. 9 Marginal probability of growth to an instability as a function of both the acceleration's pulse's amplitude, in gravity, and the acceleration pulse's frequency, in hertz.
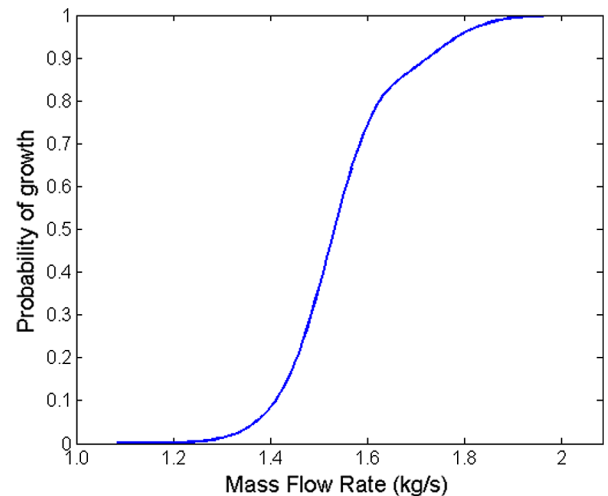

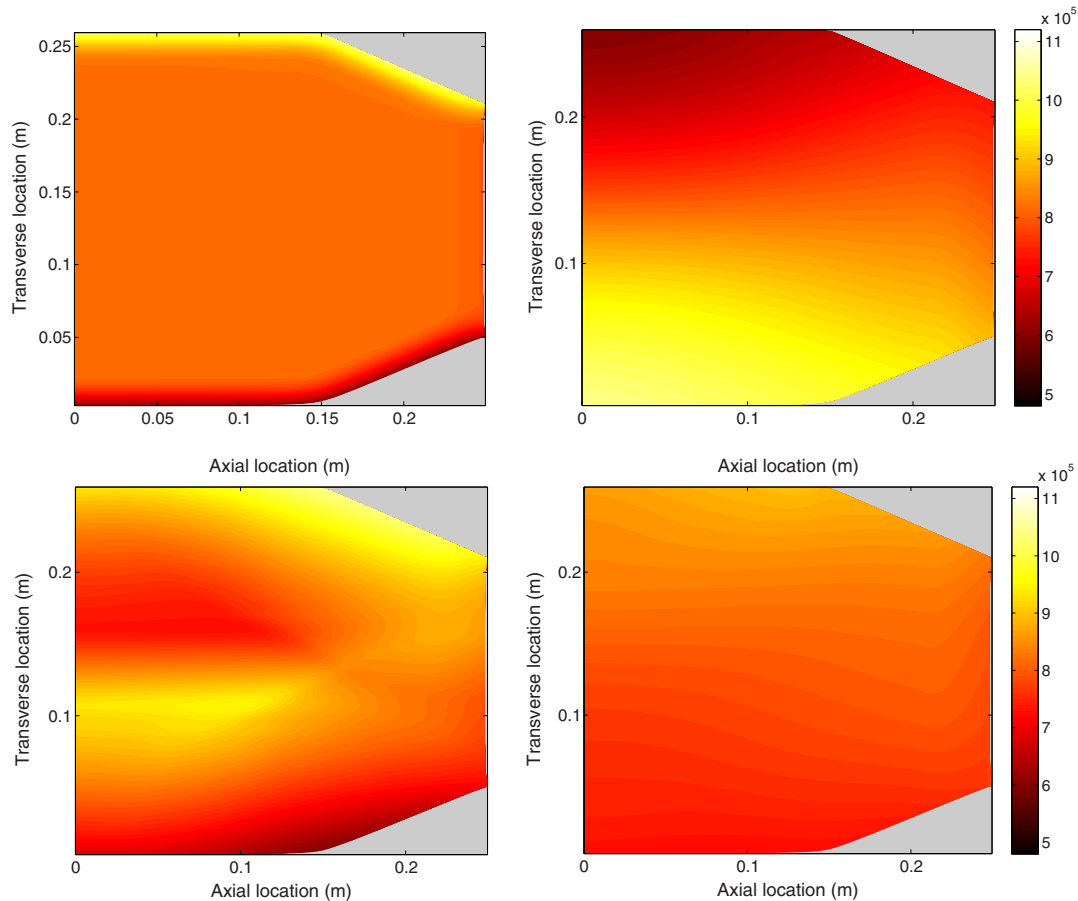Fig. 10 Marginal probability of growth to an instability as a function of the injector mass flow rate.

Fig. 11 Development and suppression of a transverse instability in the rectangular rocket engine. Top left: initial stages of instability development; top right: grown transverse instability; bottom left: second acceleration pulse disrupting the acoustic instability; bottom right: decay to standard operating conditions. Pascals are the contour units.

resultant acoustic wave has experienced by the end of the pulse, whereas increasing the pulse's amplitude does not.

Finally, the probability of growth to an instability is plotted in Fig. 8 as a function of the acceleration pulse's frequency f(Hz). We see that the probability is greatest near the first tangential acoustic mode's frequency of 2090 Hz, with frequencies above 2090 Hz exhibiting a larger probability of growth than those below 2090 Hz.

The joint marginal probability of growth as a function of both the acceleration amplitude and frequency is given in Fig. 9. In regions where both parameters imply a low (high) probability of growth, e.g., low (high) amplitude and frequency far from the first tangential, the joint marginal probability of growth is closer to zero (1) than a simple Cartesian product of the marginal probabilities would be.

Based on these results, we observe that the cylindrical rocket motor is more unstable to disturbances of larger amplitude and duration, with greater sensitivity to the former. Pulses of which the frequency is near that of the first tangential acoustic mode are most likely to trigger an instability, with some preference for pulses of frequencies higher than the first tangential than those lower than it.

V. Stochastic Acceleration of Rectangular Rocket Motor

For the rectangular rocket motor, we use the PCE scheme to test the acceleration pulses of varying amplitudes, frequencies, and for different injector total mass flow rates. Specifically, we perform a stochastic simulation over a three-dimensional sample space in which the injector mass flow rate $\dot{m}$ is distributed uniformly between the experimental value of $\dot{m} = 2.089$ and 1.08 kg/s, the frequency $f = \omega/2\pi$ is distributed uniformly between $f = 1400$ and 2600 Hz, and the acceleration pulse amplitude A_0 is distributed uniformly between $A_0 = 0$ and 220 g, with $\dot{m}$, f and A_0 being independent.

Figure 10 shows the marginal probability of growth to an acoustic instability as a function of the injector mass flow rate. As can be seen,

for the experimental value of $\dot{m} = 2.089$ kg/s, the motor is unconditionally unstable; the probability of growth is 1. On the other hand, for lower values, near $\dot{m} = 1.08$ kg/s, the probability of growth is zero, and the rocket motor is unconditionally stable. For intermediate values of the mass flow rate, we observe triggered instability, with a growth probability between zero and 1. In all cases, the triggered instability has the shape of a first transverse acoustic wave for the rectangular pressure chamber (see Fig. 11).

The dependence of stability on the frequency of the acceleration pulse is shown in Fig. 12. As can be seen in that figure, the most destabilizing acceleration pulses are those that have a frequency
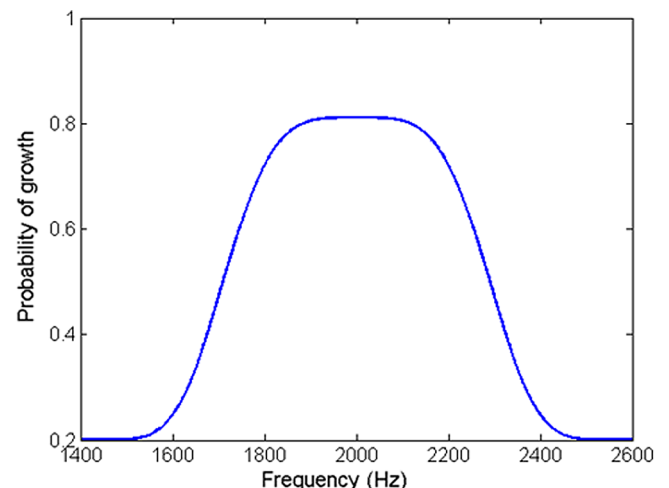

Fig. 12 Marginal probability of growth to an instability as a function of the acceleration pulse frequency, $f = \omega/2\pi$.
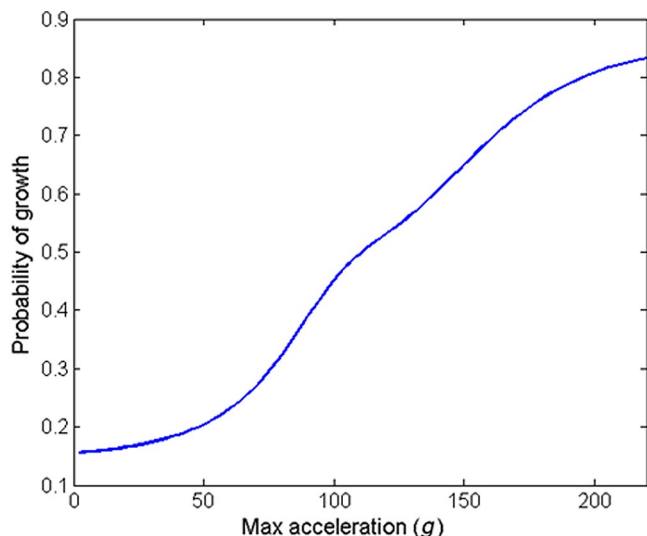
Fig. 13 Marginal probability of growth to an instability as a function of the acceleration pulse magnitude.
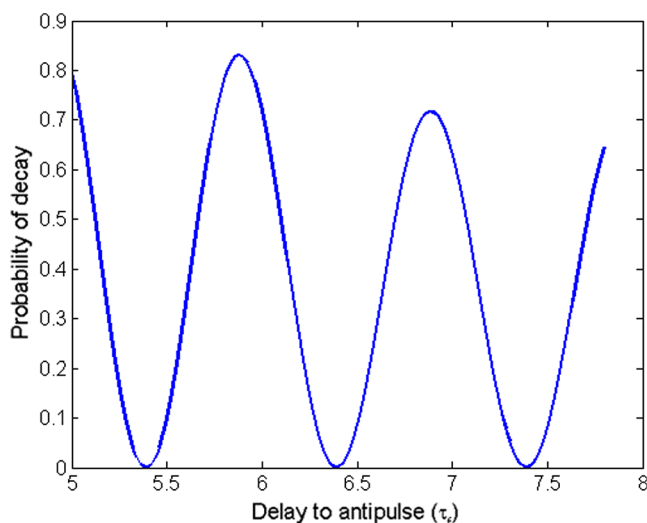

Fig. 14 Probability of instability suppression as a function of the delay between the pulse and antipulse.

around 1900 Hz, close to the frequency of the first transverse mode. Note that, even for frequencies much lower and higher than that, there is still some probability of growth, due to the presence of the unconditionally unstable cases, which will get destabilized by any perturbation.

Finally, we note in Fig. 13 that, as can be intuitively expected, the probability of growth to instability increases with increasing amplitude of the acceleration pulse. Once again, we note that the probability never reaches zero, due to the unconditionally unstable cases for the mass flow rate, and neither does it rise all the way to 1, due to the unconditionally stable cases.

In a second PCE simulation, we explore the potential for a second acceleration pulse to stabilize the rocket motor from a triggered state. Specifically, we set the frequency to $f = 1900$ Hz and the mass flow rate to $\dot{m} = 1.7$ kg/s (which is a conditionally unstable case), and we follow up the initial acceleration pulse of magnitude $A_{0,1}$ by a subsequent pulse of magnitude $-A_{0,2}$ that is initiated at a time τ after the initial pulse. The stochastic variables $A_{0,1}$, $-A_{0,2}$, and τ are independent, with $A_{0,1}$, $A_{0,2}$ being uniformly distributed between 0

and 220 g and τ uniformly distributed between $5\tau_f$ and $7.8\tau_f$, where τ_f is the period of the first transverse mode.

Figure 11 shows the initial growth of the transverse instability, and its suppression by the antipulse, for a case in which the antipulse is successful in arresting instability growth. As can be seen in Fig. 14, whether or not this is the case is highly dependent on the delay between the antipulse and the pulse; for a delay that is close to an integer number of first transverse periods, the antipulse has a high probability of restoring stability.

VI.   Conclusions

In this work, we have demonstrated the potential for whole-body acceleration pulses of a rocket engine combustion chamber to lead to the development of an acoustic instability. For both a cylindrical and a rectangular rocket engine motor, it is found that a short acceleration pulse of large amplitude, on the order of 100 g is capable of producing an acoustic instability, if its frequency is close to the chamber's acoustic frequency. For a cylindrical rocket engine, the acoustic limit cycle may be either a standing or a spinning wave, depending on the shape of the acceleration pulse. Additionally, it is seen that a subsequent pulse can also cause the decay of a growing instability, if its timing is appropriately chosen.

Acknowledgments

References

[1] Harrje, D., and Reardon, F., "Liquid Propellant Rocket Combustion Instability," NASA SP-194, U.S. Government Printing Office, 1972.

[2] Oefelein, J. C., and Yang, V., "Comprehensive Review of Liquid-Propellant Combustion Instabilities in F-1 Engines," *Journal of Propulsion and Power*, Vol. 9, No. 5, 1993, pp. 657–677.
doi:10.2514/3.23674

[3] Sirignano, W. A., and Popov, P. P., "Two-Dimensional Model for Liquid-Rocket Transverse Combustion Instability," *AIAA Journal*, Vol. 51, No. 12, 2013, pp. 2919–2934.
doi:10.2514/1.J052512

[4] Popov, P. P., Sideris, A., and Sirignano, W. A., "Stochastic Modelling of Transverse Wave Instability in a Liquid Propellant Rocket Engine," *Journal of Fluid Mechanics*, Vol. 745, 2014, pp. 62–91.
doi:10.1017/jfm.2014.96

[5] Popov, P. P., Sideris, A., and Sirignano, W. A., "Propellant Injector Influence on Liquid Propellant Rocket Engine Instability," *Journal of Propulsion and Power*, Vol. 31, No. 1, 2015, pp. 320–331.
doi:10.2514/1.B35400

[6] Shipley, K., Morgan, C., Anderson, W., Harvazinski, M., and Sankaran, V., "Computational and Experimental Investigation of Transverse Combustion Instabilities," *Joint Propulsion Conference*, AIAA, Reston, VA, 2014, pp. 1083–1099.

[7] Popov, P. P., and Sirignano, W. A., "Transverse Combustion Instabilities in a Rectangular Rocket Motor," *Journal of Propulsion and Power* (to be published).
doi:10.2514/1.B35868

[8] Pomeroy, B., "Measurement and Analysis of Combustor Response to Transverse Combustion Instability," Ph.D. Thesis, Purdue Univ., West Lafayette, ZN, 2012.

[9] Crocco, L., and Sirignano, W. A., "Effects of Transverse Velocity Components on the Nonlinear Behavior of Short Nozzles," *AIAA Journal*, Vol. 4, No. 8, 1966, pp. 1428–1430.
doi:10.2514/3.3691

[10] Westbrook, C. K., and Dryer, F. L., "Chemical Kinetic Modeling of Hydrocarbon Combustion," *Progress in Energy and Combustion Science*, Vol. 10, No. 1, 1984, pp. 1–57.
doi:10.1016/0360-1285(84)90118-7

[11] Pierce, C., and Moin, P., "Progress-Variable Approach for Large-Eddy Simulation of Non-Premixed Turbulent Combustion," *Journal of Fluid Mechanics*, Vol. 504, April 2004, pp. 73–97.
doi:10.1017/S0022112004008213